IEEE Photonics Journal
An IEEE Photonics Society Publication

Open Access

Heteroepitaxial Integration of Mid-Infrared InAsSb Light Emitting Diodes on Silicon

Volume 11, Number 3, June 2019

Evangelia Delli
Peter D. Hodgson
Eva Repiso
Adam P. Craig
Jonathan P. Hayton
Qi Lu
Andrew R. J. Marshall
Anthony Krier
Peter J. Carrington

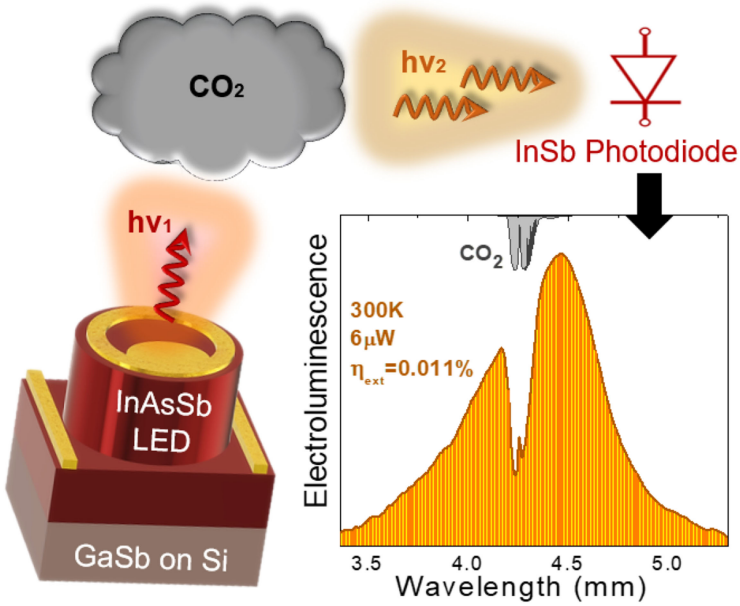

Graphic Abstract

DOI: 10.1109/JPHOT.2019.2911433

Heteroepitaxial Integration of Mid-Infrared InAsSb Light Emitting Diodes on Silicon

Evangelia Delli,[1] Peter D. Hodgson,[1,2] Eva Repiso,[2] Adam P. Craig,[2] Jonathan P. Hayton,[1] Qi Lu,[2] Andrew R. J. Marshall,[2] Anthony Krier,[2] and Peter J. Carrington[1]

[1]Department of Engineering, Lancaster University, Bailrigg LA1 4YW, U.K.
[2]Department of Physics, Lancaster University, Bailrigg LA1 4YB, U.K.

DOI:10.1109/JPHOT.2019.2911433

Manuscript received March 11, 2019; revised April 6, 2019; accepted April 11, 2019. Date of publication April 17, 2019; date of current version May 14, 2019. This work was supported in part by EPSRC under Grant EP/N018605/1, in part by the Royal Academy of Engineering under Grant 10216/114, in part by the Joy Welch Educational Charitable Trust, and in part by the Lancaster University Research Committee. Corresponding author: Peter J. Carrington (e-mail: p.carrington@lancaster.ac.uk).

Abstract: Silicon photonics has emerged as the most promising technology for next-generation compact optoelectronic systems, but further development is still required to achieve efficient and reliable on-chip light sources. Direct epitaxial growth of antimonide-based compound semiconductor materials on silicon provides a pathway toward the monolithic integration of new, mid-infrared solid-state light sources and comprehensive photonic circuits on silicon platforms. Such devices have wide-ranging applications in environmental monitoring and medical diagnostics. This paper reports on the realization of a mid-infrared InAsSb light emitting diode directly integrated onto silicon using molecular beam epitaxy. The heteroepitaxial integration of the InAsSb p-i-n device onto silicon was achieved with the use of a novel, antiphase domain-free, GaSb-on-silicon buffer layer. The device exhibited efficient light emission at room temperature, peaking at around 4.5 μm, which corresponds well to the CO_2 atmospheric absorption band. An output power of 6 μW and an external quantum efficiency of 0.011% was measured at 300 K. These results demonstrate mid-infrared III-V light emitting diodes can be directly grown on silicon, which is an essential step towards the realization of the next generation, on-chip integrated light sources.

Index Terms: InAsSb, light emitting diode, mid-infrared, molecular beam epitaxy, silicon photonics.

1. Introduction

The Mid-Infrared (MIR) spectral region from 3 to 5 μm is of immense scientific and technological interest since it contains the fundamental fingerprint absorption bands of several molecules. This affords a wide range of applications including chemical sensing, environmental monitoring and medical diagnostics. MIR silicon (Si) photonics holds the most potential for the realization of highly integrated electronic circuits, benefiting from existing, mature CMOS industrial technologies [1]. Most previous silicon-based research efforts have been targeted at devices operating in the near-infrared for datacoms and telecommunications applications, with the aim of overcoming the interconnect bottleneck [2]. In recent years, there has been increased interest in extending the operational wavelength range of Si photonics towards the mid-infrared, resulting in the development of waveguides, modulators and directional coupler devices operating at the MIR spectral region [3]. However, the indirect bandgap of Si significantly limits light emission and absorption, making

it an unsuitable material for emitter or detector applications. GeSn alloys are promising as the incorporation of tin (Sn) primarily reduces the conduction band energy at the Γ-point, resulting in a direct-bandgap semiconductor. This allows tuning of the operation wavelength across the MIR wavelength range by adjusting the Sn concentration. Short-wavelength infrared GeSn quantum well photodetectors integrated on Si have demonstrated an extended photoresponse up to 2.4 μm and a responsivity of 0.1 A/W at 2.2 μm [4]. GeSn p-n light emitting diodes grown on Ge have also been reported exhibiting an output power of 17 μW at 2.15 μm under 250 mA current [5]. However, the characteristic Sn surface segregation for alloys with high Sn content raises concerns for the suitability of the material in MIR optoelectronic systems [6]. Alternatively, integration of antimonide (Sb)-based III-V compound semiconductors on a Si platform will potentially enable on-chip realization of MIR photonic components. Such components would benefit from the advantages provided by Si substrates, including low manufacturing costs and the availability of large area wafers compared to compound semiconductor substrates such as GaSb. This is a significant advantage for fabricating focal plane arrays since the Si substrate is thermally matched to the readout integrated circuit [7]. Conventionally, off-chip integration of III-V material on Si has been realised using hybrid bonding techniques [8], [9]. However, these methods usually involve growing the III-V device separately on native substrates, and several steps of substrate thinning, material bonding and alignment are required, resulting in high fabrication costs and limited large-scale manufacturing potential. Heterogeneous integration of III-V semiconductor MIR photonic devices onto Si is thus an attractive pathway towards enabling Si platform photonics. Nevertheless, fundamental material dissimilarities have proven problematic to the direct epitaxy of III-Vs on Si: The large lattice mismatch, the polar-nonpolar character of the III-V/Si interface and differences in thermal expansion coefficient lead to the formation of various defects, such as threading dislocations (TDs) and antiphase domains (APDs) [10], which are detrimental to the device performance. However, Sb-based semiconductors have recently been grown on Si substrates by molecular beam epitaxy (MBE) using a novel strain relief technique based on interfacial misfit arrays (IMFs) formed at the III-V/Si interface. IMF arrays consist of uniformly distributed misfit dislocations and allow the immediate accommodation of misfit strain [11]. Furthermore, the use of AlSb as a surfactant on Si has also been reported to significantly improve the material quality of the epilayer as it promotes planar growth [12]. These techniques allowed the integration of III-Sb quantum cascade lasers on Si [13]. Superlattice (SL) light emitting diodes (LEDs) grown on Si have also been reported, exhibiting increased radiance compared with devices grown on GaSb as a result of improved thermal management [14]. Recently, we demonstrated a high-performance, MIR InAs/InAsSb SL photodetector on Si using an APD-free GaSb buffer layer. The novel GaSb-on-Si buffer layer was developed using an AlSb IMF growth technique and a two-temperature GaSb growth procedure, resulting in the successful confinement of most of the TDs. The use of an offcut Si wafer alongside the high temperature treatment eliminated the APDs formation. The detector demonstrated a maximum detectivity of 3.65×10^{10} Jones at 160 K, presenting high temperature performance with specific detectivity only an order of magnitude lower than state-of-the-art photodetectors integrated on native substrates [15]. These results, alongside the realization of efficient light sources, would be a large step towards the realisation of next-generation fully integrated MIR Si photonic circuits. Here, we report on the heteroepitaxial integration of a MIR InAsSb LED directly on Si using the same GaSb-on-silicon buffer layer growth approach. The room temperature peak emission wavelength was $\sim$4.5 μm with an output power of 6 μW, making these hybridised LEDs promising for the fabrication of high sensitivity CO_2 detection systems.

2. Experimental Details

The samples were grown directly on an n-type Si substrate with 4° miscut towards the [0-11] direction using a solid source Veeco GENxplor MBE system. Valved arsenic (As) and antimony (Sb) cracker cells were used to supply the group V material fluxes. An in situ, high temperature ($\sim$1000 °C) thermal cleaning procedure was employed to prepare the Si wafer surface for III-V deposition. A thin (17 ML) AlSb layer was deposited on Si leading to the formation of hemispherical,

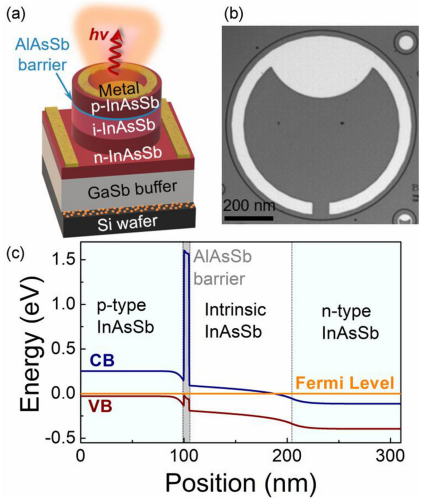

Fig. 1. (a) Schematic diagram of the InAsSb LED structure grown on Si. (b) Optical microscope image of the processed device with an 800 μm wide mesa. (c) InAsSb p-i-n band structure under zero bias conditions calculated using Nextnano [16], showing the high conduction band offset provided by the barrier layer.

non-coalesced nucleation islands. A 2 μm thick GaSb layer was then grown using a two-step growth temperature procedure (490 °C and 515 °C) resulting in a GaSb surface dislocation density of 2×10^8 cm^{-2} as measured using electron channeling contrast imaging (ECCI). Details of the Si wafer cleaning and the integration of the GaSb buffer have been described previously [15]. After the growth of the GaSb buffer layer, the wafer was cooled to 447 °C for growth of the InAsSb layers using a growth rate of 1.4 μm/hr. Two samples were grown on Si; a 3 μm thick nominally undoped InAsSb photoluminescence (PL) sample and an InAsSb p-i-n LED. A bulk, 3 μm thick, InAsSb PL reference sample on GaSb substrate was also grown. An Sb content of approximately 9% was used which is lattice matched to the underlying GaSb materials. The LED consists of a 2 μm thick n-type InAsSb layer, a 1 μm undoped InAsSb emission layer, an undoped 50 nm $AlAs_{0.06}Sb_{0.94}$. electron blocking barrier and a 500 nm thick p-type InAsSb contact layer, as shown in Fig. 1(a). The AlAsSb barrier layer provides strong electron confinement inside the intrinsic InAsSb region due to the high conduction band barrier at the InAsSb/AlAsSb heterointerface, as shown in Fig. 1(c). The n- and p-type layers were doped with Te: 6×10^{17} cm^{-3} and Be: 2×10^{18} cm^{-3} respectively. The resulting p-i-n structure was processed into LEDs with a mesa diameter of 800 μm employing standard photolithography and wet chemical etching using phosphoric acid (H_3PO_4 (1): H_2O_2 (1): H_2O (1)) and hydrochloric acid (HCL (1): H_2O_2 (1): H_2O (5)) solutions. Ring-shaped metallic contacts were formed (Fig. 1(b)) by thermal evaporation of Ti (20 nm) and Au (200 nm). Finally, the processed chips were mounted onto TO headers for testing.

High-resolution X-ray diffraction measurements were carried out using a Bede QC200 diffractometer. Photoluminescence measurements were performed on the bulk InAsSb samples using a 785 nm diode laser with 2.5 Wcm^{-2} excitation power density and a continuous flow He cryostat. Temperature dependent electroluminescence (EL) characterization of the devices was also carried using a 50% duty cycle and 1 kHz current source. A Bruker Vertex 70 Fourier Transform Infrared (FTIR) spectrometer, a 77 K InSb photodiode detector and an OptistatDN-V2 cryostat were employed for the PL and EL characterization. Electrical characterization was performed using a Lakeshore TTPX probe station, equipped with a radiation shield and a Keithley 2450 Sourcemeter. Finally, room temperature output power measurements were performed using an integrating sphere and a calibrated PbSe detector.

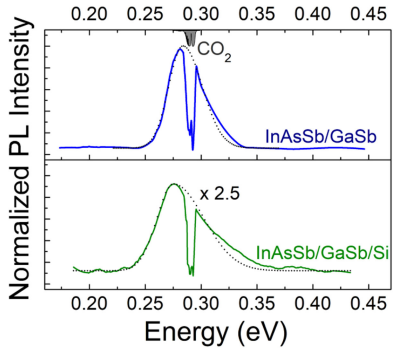

Fig. 2. Room temperature photoluminescence emission from the undoped InAsSb epitaxial layers integrated on Si and on native GaSb substrate. The dotted lines represent bi-Gaussian fitting of the spectra.

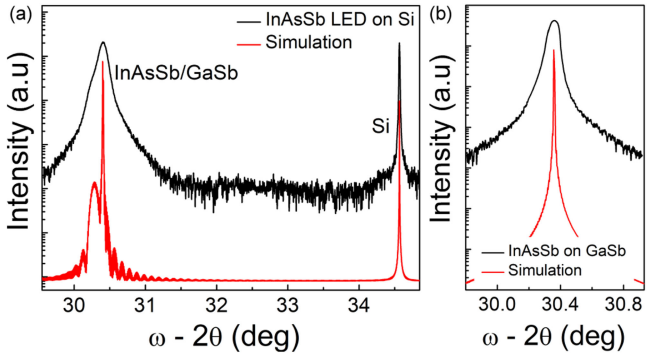

Fig. 3. Experimental and simulated high-resolution X-ray diffraction spectra of (a) the InAsSb LED (FWHM = 480 arcsec) and (b) the control InAsSb/GaSb PL sample (260 arcsec).

3. Results

Fig. 2 shows the room temperature (RT) PL emission spectra of the undoped InAsSb layers grown on GaSb and Si substrates. Both samples exhibit a high-energy tail, which is due to band filling of the low energy states and thermalisation of carriers into higher energy states, resulting in the asymmetric shape of the spectra. In this case, bi-Gaussian fits were used to determine the transition energies. The InAsSb/GaSb sample exhibited strong room temperature emission at 284 meV, in excellent agreement to the theoretically predicted bandgap energy (286.2 meV) according to Wieder and Clawson [17]. The RT PL emission signal of the InAsSb/GaSb/Si sample peaked at 275 meV and was only 2.5 times less intense than the sample grown on the GaSb substrate. These results compare favourably to previous reports of the RT PL of InAs/GaAs quantum dot structures grown on Si [18], [19], which confirms the high crystalline quality of the buffer layer. The total width of the PL peaks was also similar; 30 and 40 meV for the samples grown on GaSb and Si respectively. It is also interesting to observe that the sample grown on Si exhibited a small red shift in the PL peak position of 9 meV with respect to the one grown on GaSb. This shift can be attributed to the residual strain in the InAsSb/GaSb/Si structure as will be explained later. Furthermore, the sharp dip in the signal present in the spectra corresponds to the CO_2 atmospheric absorption in the optical path of the external light beam.

The ω-2θ high-resolution X-ray diffraction (XRD) pattern of the InAsSb p-i-n (Fig. 3(a)) indicates that the InAsSb structure is lattice matched to the GaSb buffer layer. The full width at half maximum (FWHM) of the InAsSb/GaSb peak was 480 arcsec, almost two times broader compared to the InAsSb sample grown on GaSb (Fig. 3(b)). This can be attributed to the threading dislocations in agreement with previous reports for GaSb grown on Si [20]. The small peak on the left side of the

InAsSb LED peak is attributed to the AlAsSb barrier. Simulation of the p-i-n structure XRD pattern obtained using Mercury RADS software denoted a residual tensile strain of 0.13% in the GaSb layer introduced during the post-growth cooling. The thermal expansion coefficient difference between the Si substrate and III-V structure introduces additional strain into the epilayers, resulting in lattice deformation of the GaSb [21]. The residual strain will also affect the band-gap energy of the lattice matched InAsSb, which can be modelled using the equations [22]:

$$\Delta E_c = a_c \left(2\varepsilon_{\parallel} + \varepsilon_{\perp}\right) \tag{1}$$

and

$$\Delta E_v = a_v \left(2\varepsilon_{\parallel} + \varepsilon_{\perp}\right) \tag{2}$$

for the conduction and valence band respectively. α_c and α_v are the hydrostatic deformation potential for the conduction and valence band. The biaxial and uniaxial strain is given by $\varepsilon_{\parallel}$ and $\varepsilon_{\perp}$ respectively, which is derived from the XRD using:

$$\varepsilon_{\perp/\parallel} = \frac{a_l^{\perp/\parallel} - a_l^{rel}}{a_l^{rel}} \tag{3}$$

$$a_l^{\perp} = \left(\frac{\sin(\theta_s)}{\sin(\theta_s + \Delta\theta)} - 1\right) \cdot a_s + a_s \tag{4}$$

$$a_l^{rel} = \frac{-\left(a_l^{\perp}\,(v-1) - 2v a_l^{\parallel}\right)}{1+v} \tag{5}$$

where $a_l^{\perp}$ and $a_l^{\parallel}$ is the perpendicular and parallel lattice constant of the layer, a_l^{rel} the relaxed lattice constant, a_s the substrate lattice constant, θ the xray reflection angle and v the Poisson ration. Using equations (1) and (2) it is calculated that the bandgap and emission peak energy shift by approximately 9.2 meV due to the thermally induced strain, which matches the shift in the PL emission energy (9 meV) observed earlier in Fig. 2. Similar PL behaviour has been reported previously for InP layers integrated onto Si [21].

The normalized EL emission spectra measured from one of the LEDs at various temperatures with a 190 mA drive current is presented in Fig. 4(a). The EL peak exhibits a characteristic red shift due to bandgap narrowing from 325 meV at 6 K to 278 meV at room temperature, which also broadens with increasing temperature. The peak is attributed to band-to-band recombination of carriers strongly localized in the intrinsic region of the p-i-n structure due to the high conduction band offset provided by the barrier layer. A second peak (Peak II) due to band-to-acceptor recombination is seen at lower energy at low temperatures peaking around 290 meV. As the temperature increases these levels depopulate and at temperatures higher than 120 K only the band-to-band recombination is observed. Furthermore, at room temperature the LED emission spectrum shows excellent overlap with the atmospheric CO_2 absorption at around 290 meV. The CO_2 atmospheric absorption occurred within the optical path between the cryostat and the FTIR and hence is evident in all the spectra.

The temperature dependence of the EL peak energy is shown in Fig. 4(b). The data were fitted using the Varshni equation [23]:

$$E_g(T) = E_0 - \alpha T^2/(\beta + T) \tag{6}$$

where E_0 (eV) is the band gap at 0 K, α and β are material dependent constants and T is the temperature in Kelvin. The values obtained for the Varshni fitting parameters were Eg (6 K) = 326.5 meV, $\alpha = 0.308$ meV/K and $\beta = 246$ K which are in good agreement with the results previously reported for InAsSb lattice matched on a GaSb substrate [24]. Furthermore, the slight deviation of the data points from the Varshni fit in the 0 to 30 K temperature range suggests a weak, 1.3 meV, carrier localization at low temperatures, which can be attributed to a small degree of alloy disorder.

Fig. 4(c) shows the integrated EL intensity quenching of the InAsSb LED with increasing temperature and constant input current of 190 mA. With increasing temperature from 6 K to 300 K the EL

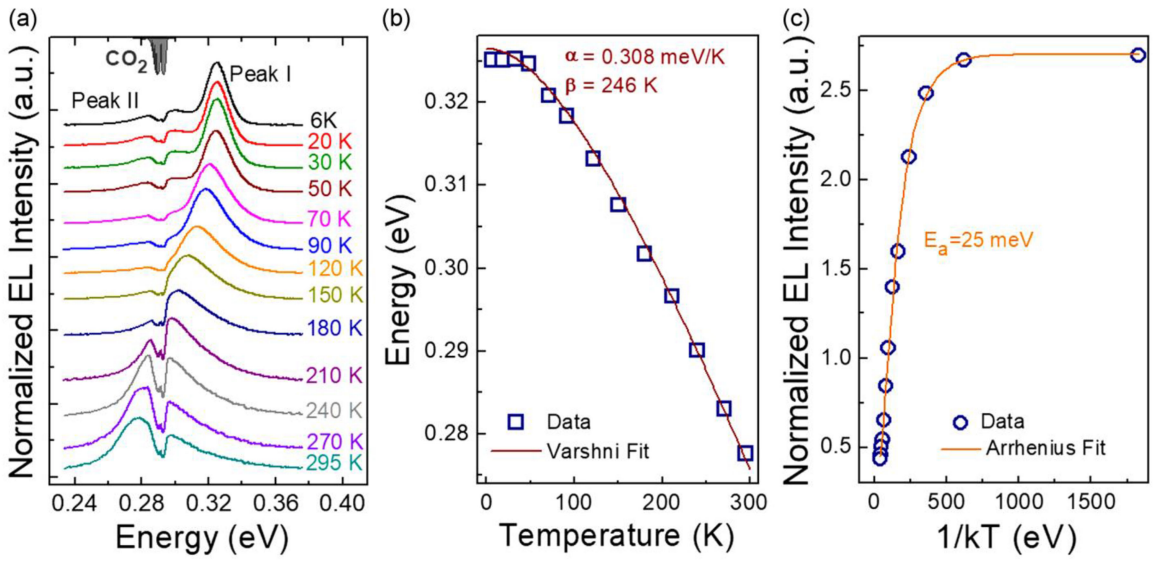

Fig. 4. (a) The temperature dependent normalized EL emission spectra obtained using 190 mA, 1 kHz and 50% duty cycle. (b) Temperature dependence of the EL emission peak and data fit using the Varshni equation. (c) Arrhenius plot of the integrated EL intensity resulting in an activation energy of 25 meV.

intensity decreased by approximately six times. The temperature dependence of the EL intensity can be described by the Arrhenius equation [24]:

$$I = \frac{I_0}{1 + A_i \exp\left(-E_i/kT\right)} \tag{7}$$

where A_i is the non-radiative recombination process coefficient and E_i is the corresponding activation energy of the process. The solid line represents the fitting of the experimental data indicating an activation energy of 25 meV. In general, the dominant non-radiative recombination processes are Shockley-Read-Hall (SRH) and Auger recombination. However, SRH recombination dominates only at low temperatures when the Fermi level lies close to the conduction band, above the trap levels. In contrast, Auger recombination processes, namely the CHCC process, presents a strong temperature dependence (increasing as $\sim T^3$). The activation energy of CHCC Auger recombination is given by the equation:

$$E^{CHCC} = \frac{m_e^* E_g}{m_e^* + m_{hh}^*} \tag{8}$$

where $m_e{}^*$ and $m_{hh}{}^*$ are the conduction and valence band carrier effective masses and E_g is the bandgap energy [25]. Using linear interpolation for the carrier effective masses, the activation energy was calculated as $E^{CHCC} = 22$ meV. This value is in excellent agreement with the experimental activation energy of the device, as calculated earlier, indicating that CHCC is the dominant quenching factor in the high temperature regime. Additionally, the CHCC Auger rate is proportional to the square of electron density [26] and it is therefore unsurprising that it dominates in the LED where the carrier concentration is high.

To investigate the room temperature output power of the device, quasi-continuous drive current conditions (1 kHz, 50% duty cycle, 190 mA) were used, resulting in a measured output power of 6 μW. The internal quantum efficiency of the device is given by the equation:

$$\eta_{int} = \frac{Pe}{h\nu i \eta_{opt}} \tag{9}$$

where $\eta_{opt} = 1/n(n+1)^2$ is the light extraction efficiency, $n = \sim 3.52$ is the refractive index of InAsSb at the device LED emission wavelength, P is the measured output power, e the electron charge,

i the drive current and hv the photon energy. Using this equation, the internal quantum efficiency was found to be 0.82%. The external quantum efficiency can be estimated using the equation:

$$\eta_{ext} = \eta_{inj} \cdot \eta_{int} \cdot \eta_{opt} \tag{10}$$

where η_{inj} is the injection efficiency which can be estimated as ~100%. The external quantum efficiency of the LED was found to be $\eta_{ext} = 0.011\%$. These results are comparable to InAsSb [27] light emitting diode grown on native GaSb. However, the internal quantum efficiency is about two times lower to that reported for AlInSb diodes grown on GaAs emitting at ~4.2 μm [28]. This confirms the usability of the GaSb/Si buffer for device integration and the excellent epitaxial crystalline quality of the lattice matched InAsSb p-i-n. The performance of the device could be improved with further optimization of the GaSb buffer layer using dislocation filters to reduce the number of threading dislocations, which currently limits the device performance. Further improvements could also be expected by using low dimensional Sb-based structures such as quantum wells and quantum dots [29] to suppress Auger recombination.

4. Conclusion

In conclusion, a MIR InAsSb p-i-n light emitting diode was heteroepitaxially integrated onto a silicon wafer using a GaSb buffer layer and exhibited bright electroluminescence at room temperature. The buffer layer confined most of the threading dislocations allowing the epitaxial growth of high crystalline quality InAsSb layers. Despite the presence of the remaining defects, the LED exhibited an external quantum efficiency of 0.011% and an output power of 6 μW under 190 mA drive current at room temperature. The electroluminescence spectrum was dominated by emission from band-to-band transitions and was coincident with the CO_2 absorption wavelength. These results demonstrate that III-V LEDs integrated onto silicon, operating in the technologically important 3 to 5 μm MIR spectral range, could enable the realization of next-generation, cost-effective light sources for sensing and monitoring systems.

Acknowledgment

The underlying data in this paper is available from https://dx.doi.org/10.17635/lancaster/researchdata/282.

References

[1] A. H. Atabaki *et al.*, "Integrating photonics with silicon nanoelectronics for the next generation of systems on a chip," *Nature*, vol. 556, pp. 349–354, 2018.
[2] M. Poulin, C. Latrasse, M.- J. Picard, Y. Painchaud, F. Pelletier, and M. Guy, "Development of silicon photonics products for telecom & datacom," in *Proc. IEEE 12th Int. Conf. Group IV Photon.*, 2015, pp. 187–188.
[3] T. Hu *et al.*, "Silicon photonic platforms for mid-infrared applications," *Photon. Res.*, vol. 5, no. 5, pp. 417–430, 2017.
[4] A. Gassenq *et al.*, "GeSn/Ge heterostructure short-wave infrared photodetectors on silicon," *Opt. Express*, vol. 20, no. 25, pp. 27297–2703, 2012.
[5] J. P. Gupta, N. Bhargava, S. Kim, T. Adams, and J. Kolodzey, "Infrared electroluminescence from GeSn heterojunction diodes grown by molecular beam epitaxy," *Appl. Phys. Lett.*, vol. 102, 2013, Art. no. 251117.
[6] L. Kormoš *et al.*, "Surface analysis of epitaxially grown GeSn alloys with Sn contents between 15% and 18%," *Surf. Interface Anal.*, vol. 49, pp. 297–302, 2017.
[7] J. W. Cairns *et al.*, "Integrated infrared detectors and readout circuits," *Proc. SPIE*, vol. 6206, 2006, Art. no. 620614.
[8] D. Liand and J. E. Bowers, "Recent progress in lasers on silicon," *Nature Photon.*, vol. 4, pp. 511–517, 2010.
[9] R. Wang *et al.*, "III–V-on-silicon photonic integrated circuits for spectroscopic sensing in the 2–4 μm wavelength range," *Sensors*, vol. 17, 2017, Art. no. 1788.
[10] S. H. Vajargah, S. Y. Woo, S. Ghanad-Tavakoli, R. N. Kleiman, J. S. Preston, and G. A. Botton, "Atomic-resolution study of polarity reversal in GaSb grown on Si by scanning transmission electron microscopy," *J. Appl. Phys.*, *vol.* 112, 2012, Art. no. 093101.
[11] J. Tatebayashi *et al.*, "Monolithically integrated III-Sb-based laser diodes grown on miscut Si substrates," *IEEE J. Sel. Topics Quantum Electron.*, vol. 15, no. 3, pp. 716–723, May/Jun. 2009.
[12] S. Hosseini Vajargah, S. Ghanad-Tavakoli, J. S. Preston, R. N. Kleiman, and G. A. Botton, "Growth mechanisms of GaSb heteroepitaxial films on Si with an AlSb buffer layer," *J. Appl. Phys.*, vol. 114, 2013, Art. no. 113101.
[13] H. Nguyen-Van *et al.*, "Quantum cascade laser grown on Si," *Sci. Rep.*, vol. 8, 2018, Art. no. 7206.

[14] A. J. Muhowski, C. L. Bogh, R. L. Heise, T. F. Boggess, and J. P. Prineas, "Improved performance of mid-infrared superlattice light emitting diodes grown epitaxially on silicon," *J. Cryst. Growth*, vol. 507, pp. 46–49, 2019.
[15] E. Delli *et al.*, "Mid-infrared InAs/InAsSb superlattice nBn photodetector monolithically integrated onto silicon," *ACS Photon.*, vol. 6, no. 2, pp. 538–544, 2019.
[16] [Online]. Available: https://www.nextnano.de/index.php
[17] H. H. Wieder and A. R. Clawson, "Photo-electronic properties of $InAs_{0.07}Sb_{0.93}$ films," *Thin Solid Films*, vol. 15, no. 2, pp. 217–221, 1973.
[18] Y. Wan, Q. Li, Y. Geng, B. Shei, and K. M. Lau, "InAs/GaAs quantum dots on GaAs-on-V-grooved-Si substrate with high optical quality in the 1.3 μm band," *Appl. Phys. Lett.*, vol. 107, 2015, Art. no. 081106.
[19] J. R. Orchard *et al.*, "In situ annealing enhancement of the optical properties and laser device performance of InAs quantum dots grown on Si substrates," *Opt. Express*, vol. 24, no. 6, pp. 6196–6202, 2016.
[20] A. P. Craig, P. J. Carrington, H. Liu, and A. R. J. Marshall, "Characterization of 6.1 Å III-v materials grown on GaAs and Si: A comparison of GaSb/GaAs epitaxy and GaSb/AlSb/Si epitaxy," *J. Cryst. Growth*, vol. 435, pp. 56–61, 2016.
[21] M. Sugo, N. Uchida, A. Yamamoto, T. Nishioka, and M. Yamaguchi, "Residual strains in heteroepitaxial III-V semiconductor films on Si (100) substrates," *J. Appl. Phys.*, vol. 65, 1989, Art. no. 591.
[22] M. P. C. M. Krijn, "Heterojunction band offsets and effective masses in III-V quaternary alloys," *Semicond. Sci. Technol.*, vol. 6, pp. 27–31, 1991.
[23] K. P. O'Donnel and X. Chen, "Temperature dependence of semiconductor bandgaps," *Appl. Phys. Lett.*, vol. 58, 1991, Art. no. 2924.
[24] S. Elies, A. Krier, I. R. Cleverley, and K. Singer, "Photoluminescence of MBE-grown $InAs_{1-x}Sb_x$ lattice matched to GaSb," *J. Phys. D, Appl. Phys.*, vol. 26, pp. 159–162, 1993.
[25] J. A. Keen, D. Lane, M. Kesaria, A. R. J. Marshall, and A. Singer, "InAs/InAsSb type-II strained-layer superlattices for mid-infrared LEDs," *J. Phys. D, Appl. Phys.*, vol. 51, 2018, Art. no. 075103.
[26] A. Rogalski, K. Adamiec, and J. Rutkowski, *Narrow-Gap Semiconductor Photodiodes*. SPIE Press, Bellingham, Washington, pp. 98227–6202, 2000.
[27] Y. Mao and A. Krier, "Uncooled 4.2 μm light emitting diodes based on $InAs_{0.91}Sb_{0.09}$/GaSb grown by LPE," *Opt. Mater.*, vol. 6, pp. 55–61, 1996.
[28] M. K. Haigh, G. R. Nash, S. J. Smith, L. Buckle, M. T. Emeny, and T. Ashley, "Mid-infrared $Al_xIn_{1-x}Sb$ light-emitting diodes," *Appl. Phys. Lett.*, vol. 90, 2007, Art. no. 231116.
[29] P. J. Carrington, V. A. Solov'ev, Q. Zhuang, A. Krier, and S. Ivanov, "Room temperature midinfrared electroluminescence from InSb/InAs quantum dot light emitting diodes," *Appl. Phys. Lett.*, vol. 93, 2008, Art. no. 091101.